processes

Article

Thermal Conductivity Measurement System for Functional and Structural Products

Nikolai S. Morozov *, Viktor Yu. Gubin, Dmitriy V. Vakhrushin, Maxim S. Konstantinov, Roman A. Minushkin, Alexandra V. Gracheva, Sergei N. Chebotarev and Viktor V. Avdeev

Department of Chemistry, Lomonosov Moscow State University, Moscow 119991, Russia; classic_fond@mail.ru (V.Y.G.); vakhrushin_dmitry@mail.ru (D.V.V.); konstantinov.maxim2040@yandex.ru (M.S.K.); minushkinroman@yandex.ru (R.A.M.); gracheva.a@inumit.ru (A.V.G.); chebotarev.s@inumit.ru (S.N.C.); avdeev@highp.chem.msu.ru (V.V.A.)
* Correspondence: morozov.n@inumit.ru

Abstract: An automated system for measuring the thermal conductivity of functional and structural materials was developed. The main building blocks of the setup are the following: heating unit and cooling unit creating a heat flux gradient in the test sample; thermal resistances for temperature registration and control; and thermal pads for better contact between parts of the setup and the sample. The effect of the thermal conductivity of thermal pads and thermal resistances on the distribution of thermal fields in the developed setup was studied by computer modelling. A control software for the measuring setup was developed based on the hardware implementation of the steady-state Fourier's law-based method for the determination of thermal conductivity. The stopping criterion for the setup control software is the equality of heat fluxes in the heating and cooling units, as well as the stability of the thermal conductivity coefficient readings. The testing and calibration of the device were carried out using a sample of pure aluminum (99.999 wt.% Al). It was found that the experimental value of the thermal conductivity coefficient of the aluminum sample at room temperature (T = 22 °C) is $<\lambda> = 243 \pm 3$ W/m·K. This value of the thermal conductivity coefficient is consistent with the literature data and experimental values obtained by the laser flash method, which ranges within λ = 210–260 W/m·K.

Keywords: thermal conductivity coefficient; temperature; heat flux; heating unit; cooling unit; thermal resistances; thermal pads

check for updates

Citation: Morozov, N.S.; Gubin, V.Y.; Vakhrushin, D.V.; Konstantinov, M.S.; Minushkin, R.A.; Gracheva, A.V.; Chebotarev, S.N.; Avdeev, V.V. Thermal Conductivity Measurement System for Functional and Structural Products. *Processes* **2024**, *12*, 2219. https://doi.org/10.3390/pr12102219

Academic Editor: Masoud Soroush

Received: 19 September 2024
Revised: 7 October 2024
Accepted: 10 October 2024
Published: 11 October 2024

1. Introduction

Knowledge of thermophysical properties is important in science, technology, industry for creating and manufacturing new and improving existing materials [1]. One of the key thermal properties is thermal conductivity, which can be used to characterize the efficiency of thermal engineering systems or devices [2].

The many ways to measure the thermal conductivity coefficient can be divided into two groups: steady-state and non-steady-state [3]. The methods vary in their range of applicability and have both advantages and disadvantages.

Stationary methods of thermal conductivity measurements are based on the concept of a steady-state heat flux, i.e., imply the independence of the temperature from time in each point of the sample [4]. Based on this, the thermal conductivity coefficient can be calculated.

At the moment, experiments in a steady-state regime are carried out using both self-made experimental setups [5–7] and commercially available instruments. For example, the Netzsch GHP 456 Titan instrument (Selb, Germany) [8,9] measures the thermal conductivity of plates or bars with dimensions up to 300 mm × 300 mm and up to 100 mm thick in the temperature range from −160 to 620 °C, and the HFM 446 Lambda instrument [10,11] measures the thermal conductivity of plates or bars up to 203 mm × 203 mm in size and up to 51 mm thick in the temperature range from −20 to 90 °C. The FOX 314 Thermal Conductivity Heat Flow Meter manufactured by TA Instruments Waters Corporation (New Castle, DE, USA) [12–14] measures the thermal conductivity of plates or bars sized up to 250 mm × 250 mm and up to 50 mm thick in the temperature range from −20 to 75 °C. The HFM 300 instrument by Linseis (Selb, Germany) [15,16] measures the thermal conductivity of plates or bars up to 300 mm × 300 mm in size and up to 100 mm thick in the −35 to 90 °C temperature range.

Steady-state approaches are advantageous in terms of: simple design; direct relation of measurement results to the physical law of thermal conductivity; high measurement accuracy due to the minimization of the time factor contribution; a wide range of applications; stability of experimental conditions; and reliability and repeatability of results. The disadvantages of steady-state methods are: time-consuming experiments; the necessity of having large samples; high sensitivity to the sample geometry; and the need to account for the thermal losses due to heat exchange with the environment.

One of the most common non-steady-state methods for measuring thermal conductivity are the laser flash [17] and the hot disk [18,19] methods. These thermal conductivity measurement techniques are based on the analysis of the material temperature response to temporary thermal disturbances. Unlike steady-state methods, where the temperature gradient remains constant, non-steady-state methods consider how the sample temperature changes over time after a thermal pulse or periodic signal is applied. The thermal conductivity coefficient can be derived from the analysis of the time dependence of the temperature (thermal conductivity), as well as of the properties of the studied material (density and heat capacity).

Among the devices for measuring thermal conductivity coefficient, instruments based on laser flash method are common, such as those of the LFA-427 [20], LFA-447 [21], and LFA-467 [22–24] series manufactured by Netzsch (Selb or Bremen, Germany; and Yokohama, Japan). The test samples are usually cylinders of 6–25 mm in diameter, up to 6 mm high, and the available temperature ranges from −125 to 2800 °C (depending on the study purposes and instrument configuration). Instruments of the DXF-200 [25], DXF-500 [26], and DXF-900 [27] series produced by TA-Instruments (New Castle, DE, USA) are also widely used. Typically, the test samples are cylinders of 8–25 mm in diameter, up to 10 mm thick. Measurements are conducted in the temperature range from −175 to 900 °C (depending on the study purposes and instrument configuration). Also widespread have become the Linseis instruments (Selb, Germany) of the LFA–1000 [28] and LFA–1600 [29] series. Here, the measured samples are cylinders of 3–25 mm in diameter and up to 6 mm thick. Measurements are carried out at temperatures from −125 to 1600 °C (depending on the study purposes and instrument configuration).

Another widely known technique for the determination of thermal conductivity coefficient is the hot disk method. Laboratory-made experimental setups and designs are mainly used here, which are based on a disk sensor manufactured by TPS Kapton (Goteborg or Uppsala, Sweden) [30,31], working in the temperature range from −253 to 1000 °C. Sensors from C-Therm Technologies Ltd. (Fredericton, NB, Canada) are available on the market [32,33], with their operating temperature range being similar to that of TPS Kapton instruments. There are also full-fledged instruments commercially available from the Hot Disk Instruments company, such as TPS 500S [34], TPS 1500 [35], TPS 2500/TPS 2500S [36,37], and TPS 3500 [38,39]. Measurements can be conducted at temperatures from −253 to 1000 °C (depending on the study purposes and instrument configuration). The sample size is limited by the instrument dimensions. SKZ 1061C TPS instruments manufactured by SKZ Industrial (Jinan, China) are also used [40,41]. However, they have a narrow operating temperature range (from 18 to 130 °C), allow a maximum sample diameter of 15 mm, and thickness of about several millimeters.

Other generally accepted and effective non-stationary methods for measuring the thermal conductivity of materials are also known: the temperature wave analysis (TWA) [42] method and the laser spot thermography method (LST) [43,44].

The advantages of non-steady-state approaches are: higher measurement throughput as compared to steady-state methods; smaller geometric dimensions of samples as compared to steady-state methods; the possibility of testing materials with a low thermal conductivity; and the possibility of studying the temporal characteristics of thermal conductivity. The drawbacks of non-steady-state methods are that the heat capacity needs to be measured in advance; the mathematical models and computational methods for interpreting the results are complex; the results are sensitive to experimental conditions; contact resistance between sample and sensor, as well as sample inhomogeneities, cause difficulties; and that the requirements for the accuracy of equipment calibration are high.

The analysis of the literature and the instrumentation market has shown that devices (mainly commercial instruments) measure the thermal conductivity coefficient of the material itself. However, specific products, due to their special form and design, may have a different thermal conductivity coefficient than the material itself. Such products are often used in aviation, oil and gas, chemical, energy (including nuclear), and other industries. They are used, e.g., for abstracting and dissipating heat in the bulk of the material. Therefore, an urgent task is to develop a device for measuring the thermal conductivity coefficients of structural and functional extended products (made of steel, aluminum, copper, titanium, graphite, silicon carbide, and tungsten carbide) based on a simple and efficient steady-state Fourier method.

In this paper, we describe the automated system developed for measuring the thermal conductivity of functional and structural products with the help of computer modelling and discuss the obtained results in comparison with other studies.

2. Design Features of the Setup

2.1. Main Components of the Setup for Thermal Conductivity Measurements

The main components of the developed setup are the following (Figure 1):

(1) The heating unit (1) comprises a ceramic heating element (8), a thermally conductive copper element (9) for balancing the heat flux, and thermal resistances (5) to control the input thermal flux. The unit is thermally insulated in order to prevent heat exchange with the environment.

(2) The cooling unit (2) comprises a Peltier element (10) with a water-cooling system, a thermally conductive copper element (9) for balancing the heat flux, and thermal resistance (5) to control the output heat flux. The unit is thermally insulated in order to prevent heat exchange with the environment.

(3) The central unit (3) includes a compartment for an experimental sample (4), whose thermal conductivity needs to be measured, and thermal resistances (5) with a special mechanism for moving them (6). The compartment is thermally insulated in order to prevent heat exchange with the environment. The experimental sample has precise dimensions of 40 mm in width, 40 mm in height, and 300 mm in length.

The heating and the cooling unit are connected to the test sample by thermally conductive pads (7) maximizing the unit-sample contact area (which depends on clamping force) and thus ensuring that less heat is lost in the contact area.

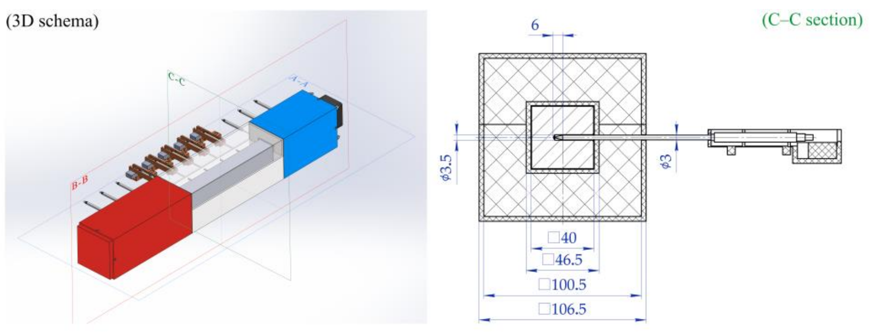

Figure 1. *Cont.*

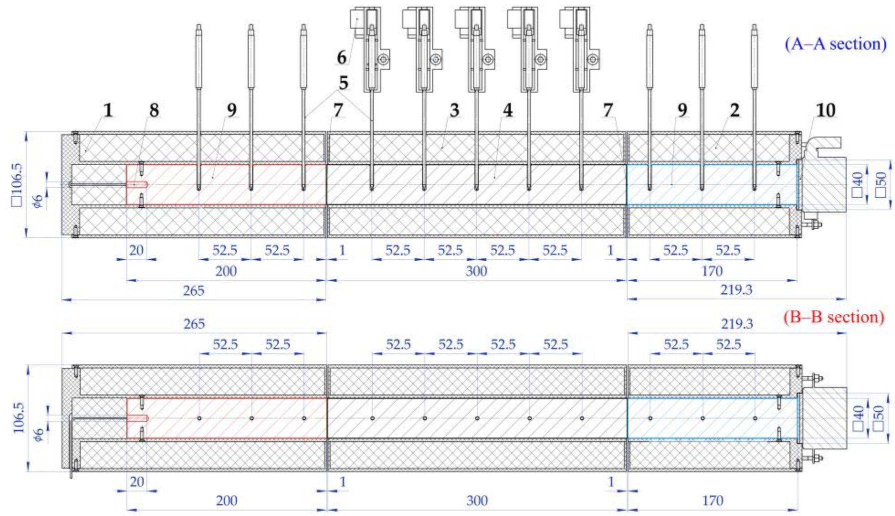

Figure 1. Schematic diagram of the setup: A–A, B–B, and C–C sectional drawings of the setup.

2.2. Conceptual Scheme of the Thermal Conductivity Measurement Process

The device developed for measuring the thermal conductivity coefficient is built according to the principles of Fourier's law-based steady-state-mode thermal conductivity measurement (Equation (1)) [45]. The proportionality coefficient, λ, is termed the thermal conductivity coefficient and characterizes the ability of a body to conduct heat. The "–" sign means that the heat flux is directed towards the lower temperature region.

$$\mathbf{q} = -\lambda \nabla T \tag{1}$$

where **q** is the heat flux vector and ∇T temperature gradient.

The test sample is placed between the heating unit (Figure 1, red zone) and the cooling unit (heat sink, Figure 1, blue zone) having different temperatures, which are kept constant during the measurement. The contact area is maximized by thermal pads. The ceramic heater creates a heat flux flowing from the heating unit to the cooling unit through the experimental sample. The measurement of temperatures of the heating unit, the sample, and the cooling unit is controlled by thermal resistances. Within one hour, the steady-state mode is reached, i.e., a uniform temperature establishes across the sample, at which the thermal conductivity coefficient is to be measured.

According to Equation (1) and the design of the developed automated system (Figure 1), the thermal conductivity coefficient can be calculated using Equation (2):

$$\lambda = \frac{Q \cdot \Delta l}{S \cdot (T_1 - T_2)} \tag{2}$$

where Q is the steady-state heat flux going through the sample; Δl is the distance between the opposite thermal resistances in the sample; S is the sample cross-sectional area; T_1 is the sample temperature on the side of the heater unit; and T_2 is the sample temperature on the side of the cooling unit.

In order to obtain accurate measurement results, as well as to reduce the errors, the following changes are necessary in the setup design and the experimental procedures:

(1) The use of high-precision thermal resistances;
(2) Thermal insulation of the heating unit, the sample, and the cooling unit of the experimental setup for minimizing heat losses;
(3) Hardware calibration;
(4) Testing reference samples, as well as conducting replicate measurements.

2.3. Specifications of Structural Materials and the Setup Components

The principal structural elements and materials of the developed automated system are shown in Figure 2.

(a) The heating system supplies a certain amount of heat to create a stable heat flux from the heater unit to the cooling unit through the experimental sample. It is a cylindrical ceramic element with a power of P_{max} = 60 W, capable of heating to a maximum temperature of T_{max} = 400 °C.
(b) Thermal resistance is a device for measuring temperature. It has a pin-shaped form and contains a platinum thermosensitive element in a housing made of corrosion-resistant AISI 321 steel. The operating temperature range is T_{work} = −50. . .+250 °C.
(c) Thermal pad is a material ensuring the maximum area of contact and efficient heat transfer between the units and the sample. It is a 40 × 40 × 1 mm plate with a thermal conductivity coefficient λ = 20 W/m·K. The thermal pad's operating temperature range is T_{work} = −40. . .+200 °C.
(d) The cooling system removes a certain amount of heat to create a stable heat flux from the heater unit to the cooling unit through the experimental sample. It is a Peltier element in a ceramic case with a maximum power of P_{max} = 236 W. The operating temperature range is T_{work} = −50. . .+100 °C.
(e) Thermal insulation provides a significant reduction in heat loss to the environment. It is an extruded polystyrene foam with a thermal conductivity coefficient λ = 0.030 W/m·K. The operating temperature range is T_{work} = −50. . .+80 °C.
(f) The heat removal system comprises a copper plate mounted on the "hot" surface of the Peltier element, and an aluminum radiator cooled by two (or three) fans of the 120 × 120 × 25 mm size.

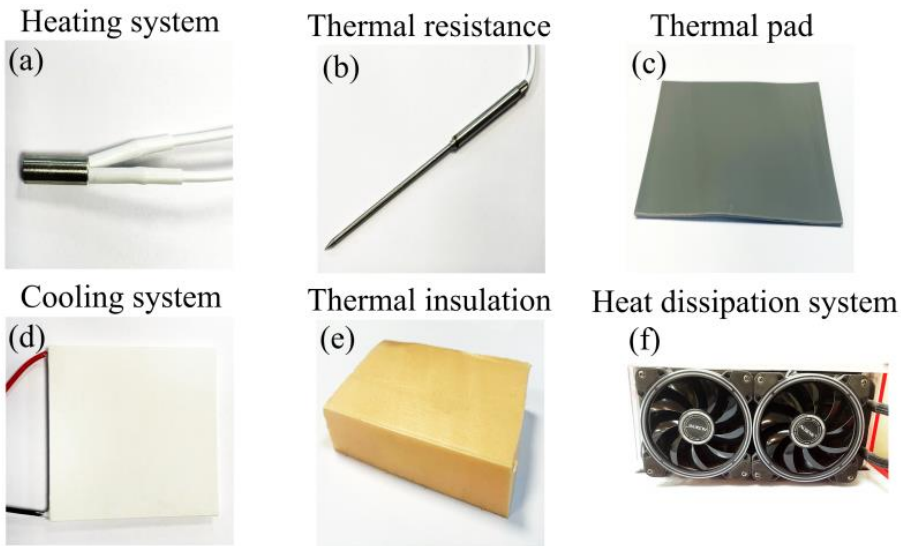

Figure 2. Main structural elements and materials.

3. Modelling of the Distribution of Thermal Fields of and Fluctuations in Heat Fluxes Depending on the Design Features of the Setup

3.1. Formulation of the Problem for the Modelling of Thermal Processes

In order to measure the thermal conductivity coefficient as accurately as possible, it is important to find the optimal operating mode of the thermal conductivity measurement setup and estimate the instrumental error. These tasks can be solved with the help of mathematical modelling, which makes it possible to study the distribution of heat fluxes in the experimental sample and thermal fields in the working area of the setup as a function of various parameters in the developed model [46–48].

The heat transfer process consists of a set of phenomena influenced by various factors [49–51]. This makes the calculations quite complicated. To reduce the complexity of the problem and increase the efficiency of calculations, it is necessary to simplify the mathematical model, eliminating the least important factors. Seeking the reliability and realism of the calculation results, the following assumptions were made.

(1) The setup components are in complete contact, with no accounting for the roughness of the surfaces.
(2) Since the setup operates under moderate temperatures (below 100 °C), radiative heat transfer was not taken into account.
(3) The model supposes the heating element to be a cylinder, and heat is released in the bulk of it.
(4) The model supposes the Peltier element to be a surface with a heat flux power equal in absolute value to the power of the heating element, but with the opposite sign.

The mathematical treatment is based on the heat transfer Equation (3):

$$\rho c_p \frac{\partial T}{\partial t} + \nabla \mathbf{q} = Q^* \tag{3}$$

where ρ is the material density; c_p is the specific heat capacity of the material; Q^* is the quantity of heat from additional sources; and λ is the thermal conductivity coefficient.

To solve this partial differential equation, the finite element method (FEM) was used, which implies dividing the computational domain into separate parts, in which the sought values of functions are determined by approximation [52,53]. Note that the contact between the materials is considered complete, so that the jumps of functions at the interface were assumed to be zero.

Equations (4)–(8) determined the boundary and initial conditions.

Boundary conditions:

(1) On the outer surface of heat insulation:

$$\begin{cases} -\mathbf{n}\cdot\mathbf{q} = q_0 \\ q_0 = h(T_{ext} - T)' \end{cases} \tag{4}$$

where h is the heat transfer coefficient; T_{ext} is the ambient temperature; T is the temperature on the sample; and $\mathbf{n}$ is the normal vector to the boundary.

(2) On the surface of the Peltier element:

$$\begin{cases} -\mathbf{n}\cdot\mathbf{q} = q_0 \\ q_0 = P_0/A' \end{cases} \tag{5}$$

where P_0 is the Peltier element power; and A is the cooling unit surface area.

(3) In the bulk of the heating element:

$$\begin{cases} Q^* = Q_0 \\ Q_0 = P_0/V' \end{cases} \tag{6}$$

where Q is the volumetric heat release (W/m^3); P_0 is the heating element power; and V is the heating element volume.

(4) At the interface of two different materials in the setup:

$$\begin{cases} T_+ = T_- \\ \lambda_+\left(\frac{\partial T_+}{\partial n}\right) = \lambda_-\left(\frac{\partial T_-}{\partial n}\right)' \end{cases} \tag{7}$$

where T_+ and T_- are local temperatures from the side of the first and the second materials, respectively; and λ_+ and λ_- are the local thermal conductivity coefficients from the side of the first and the second materials, respectively.

Initial conditions:

$$T_0 = T_{amb} \tag{8}$$

where T_{amb} is the room temperature.

3.2. Simplified 3D Model for the Calculation of Thermal Fields

The working area of the setup was modelled to calculate the thermal fields of the sample. The first model was divided into five zones: heating zone, sample area, cooling zone, and two thermal pad areas. In the heating zone, there is a heating element, a cylinder for which the condition of volumetric thermal radiation with a certain power was set (Equation (6)). At the boundary of the cooling zone, there is a Peltier element, for which the heat flux removal condition was set; the flux should be equal in absolute value to the heating flux (Equation (5)). The working area of the setup is thermally insulated. A condition to account for heat transfer to the environment was set for the outer surfaces of thermal insulation (Equation (4)). Calculations at the interface of two different materials implied the continuity of temperature and heat flux (Equation (7)). The initial conditions corresponded to heating the sample to room temperature (Equation (8)).

The original model was complicated by the introduction of thermal resistances to the setup in order to assess heat flux changes (the second model, Figure 3). To compare the simulation results with the experimental data, the temperature differences between points No. 1 and No. 5 were calculated.

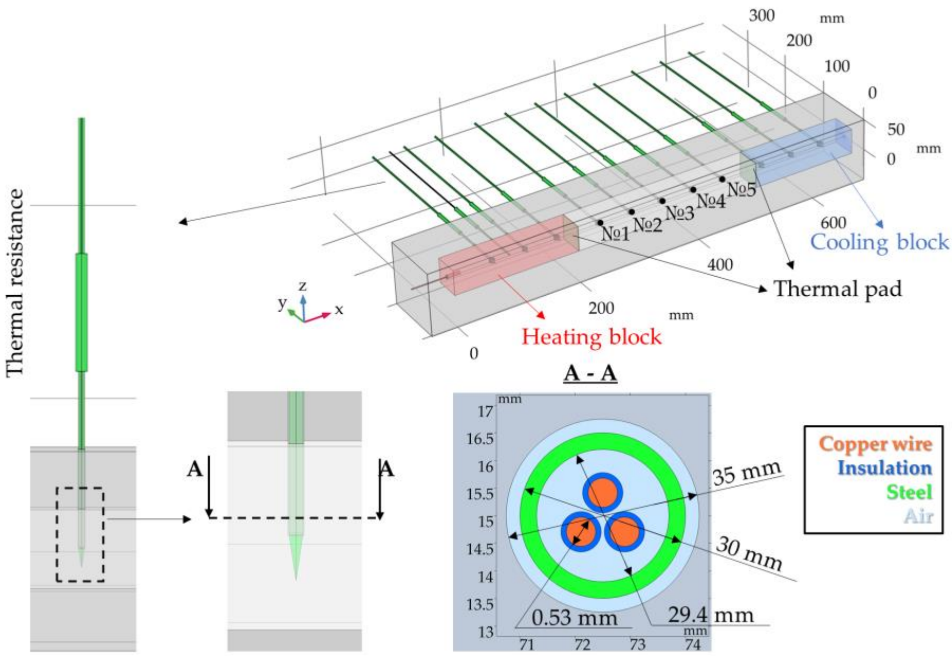

Figure 3. Geometry of the model setup.

3.3. Temperature Distribution According to the Change in Heat Fluxes

Calculations using the first model were conducted for different heat fluxes, i.e., various temperature differences $\Delta T_{1\text{-}5}$ between points No. 1 and No. 5 on the sample (Figure 4a). The estimation of the $\Delta T_{1\text{-}5}$ parameter is necessary to determine the optimal operating mode of the setup. We varied the temperature difference by changing the power of the heating and the cooling units. The setup was considered to work in a steady-state mode when the temperature fluctuations were lower than 0.1 °C, because this large difference was the measurement error of our temperature-recording devices.

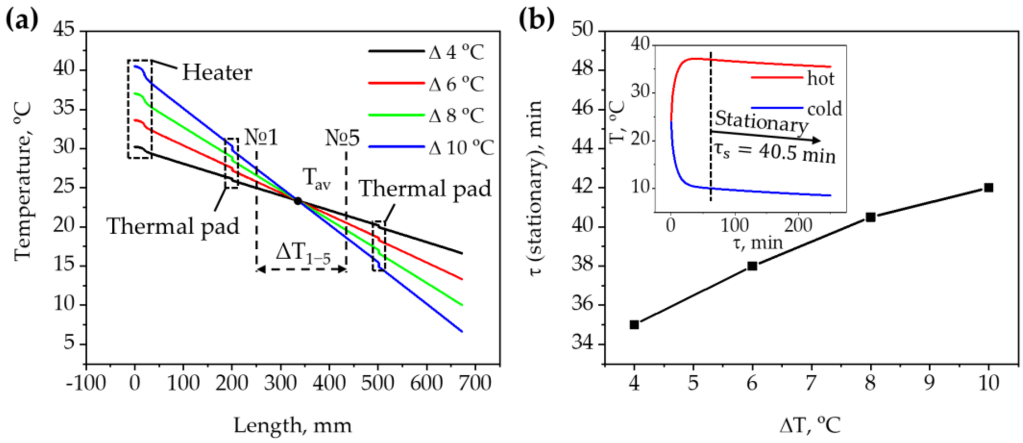

Figure 4. Simulation results obtained by varying the temperature difference between the first and the fifth thermal resistance on the sample surface: the curves of temperature distribution along the length of the working area (**a**) and stabilization time of the setup (**b**).

The curves of the temperature distribution along the length of the working area (Figure 4a) are linear in general, with non-linear regions reflecting the effect of the heating unit and the thermal pads on the distribution. The sample middle point temperature, T_{av} (the temperature in the middle of the sample in the presence of heat flux), decreased from 23.1 to 22.6 °C with an increase in $\Delta T_{1\text{-}5}$ from 4 to 10 °C.

Another important parameter characterizing the efficiency of the setup is the stabilization time. As $\Delta T_{1\text{-}5}$ increased (Figure 4b), an increase in heat flux was observed, which led to an increase in the time required for the setup to reach its operating conditions. This behavior is explained by the fact that more time is necessary to create a larger temperature gradient. The inset in Figure 4b shows an example of a stabilization process curve for the temperature difference $\Delta T_{1\text{-}5}$ = 8 °C. The operating regime is driven by the stabilization of heat flows, both in the heating unit (red line) and in the cooling unit (blue line), which are described by linear functions (with temperature fluctuations are lower than 0.1 °C). An additional condition for a steady state was the parallelism of these dependences during heating and cooling. The slight drop of fluxes after reaching the steady-state mode is due to losses of heat to the environment.

3.4. Effect of Thermal Conductivity of Thermal Pads on Temperature Distribution

The use of thermal pads is necessary to create a tighter contact and ensure efficient heat transfer between the sample and the heating or cooling unit. When choosing thermal pad material, it is important to understand its effect on the change in the temperature field and, consequently, on the setup operation (Figure 5). Therefore, the thermal conductivity coefficient of the thermal pad (λ_{tp}) is one of the important characteristics. Calculations using the first model were carried out to study thermal characteristics for various λ_{tp} values.

The thermal conductivity coefficient of thermal pads does not affect the form of the temperature distribution and the resulting thermal conductivity coefficient of the sample (Figure 5a), but has a significant effect on the temperature jump at the interfaces of the heating and cooling units with the sample (Figure 5a). As the thermal conductivity coefficient increases from 5 W/m·K to 50 W/m·K, the temperature difference at the heating unit/sample interface (ΔT_{tp}) decreases from 2.3 °C to 0.2 °C (Figure 5b). It follows that, at higher values of λ_{tp}, the heat loss will be lower, and the middle point temperature T_{av} will be higher.

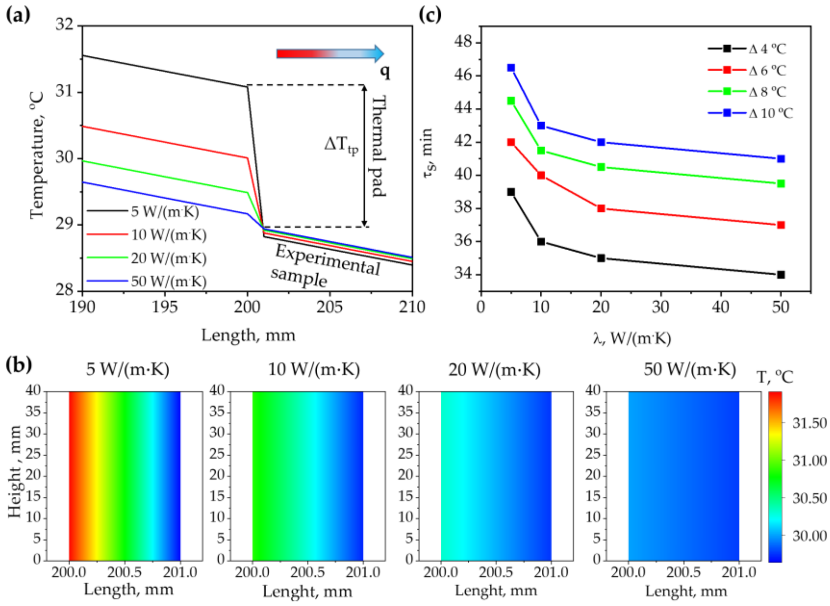

Figure 5. Results of modelling with variable thermal conductivity coefficient of thermal pads: change in the temperature in the setup with different thermal conductivity values of the thermal pads (**a**) and temperature difference at the interface heating unit/sample (**b**), and the setup stabilization time (**c**).

Numerical modelling has shown that the thermal conductivity coefficient of the thermal pad influenced the setup stabilization time (Figure 5c). For different heat fluxes in the sample, the time required for the setup to reach its operating conditions decreases with an increase in λ_{tp}.

3.5. Distribution of Thermal Fields in the Presence of Thermal Resistances

One of the primary tasks of instrumentation engineering is to ensure the accuracy of the obtained experimental data, as well as to assess the contribution of the setup instrumental error to measured values. To this end, the temperature distribution in the working area of the setup was compared in two models—with thermal resistances (the second model) and without them (the first model) (Figure 6a,b). Thermal resistances and their internal components are connected to the surrounding environment and thus can additionally remove heat from the experimental sample during the setup operation. To illustrate the effect of thermal resistances on thermal fields in the sample, temperature profiles are presented along the sections of the setup working area (Figure 6a,b), going through the middle of the setup working area at z = 20 mm (1), tangentially to the thermal resistances at z = 25 mm (2), and along the sample side wall at z = 40 mm (3).

The analysis of the modelling results revealed minor disturbances in the temperature field in the area near thermal resistances (Figure 6c). This is due to heat transfer into the air from the outer part of a thermal resistance. The change in the temperature distribution can be detailed using the sample cross-sections at the locations of thermal resistances. In the presence of thermal resistances, one can clearly see the distortion of temperature fields in sections going through the heating and the cooling units at points No. 1 and No. 5, respectively.

The temperature inside the thermal resistance differs by 2 °C from the sample temperature. This difference is due to a change in the temperature gradient in passage through materials with differing thermal conductivity coefficients ($\lambda_{Al} >> \lambda_{air}$), since the heat flux moves across air regions (gaps in the sample and in the inner part of the thermal resistance housing) several times in passing along the sample. The results of the numerical simulation of the effect of thermal resistances on the temperature in the sample at variable powers of the heating and cooling units are shown in Table 1.

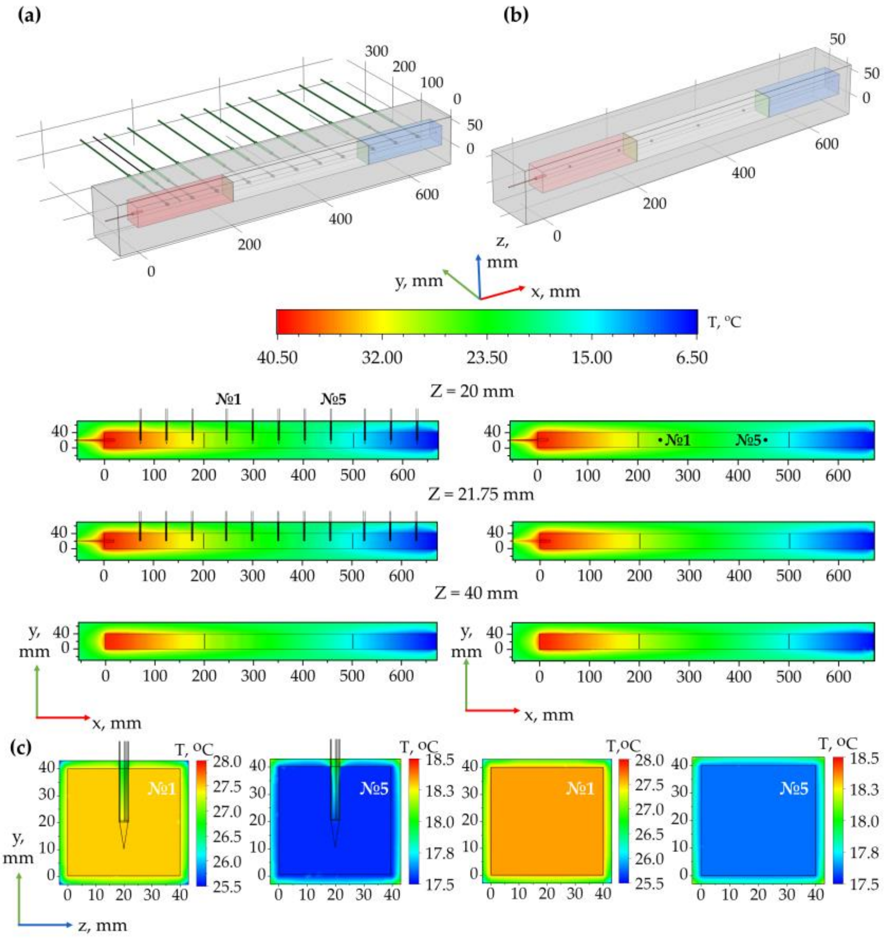

Figure 6. Comparison of the temperature distribution over the working area of the setup without (**a**) and with thermal resistances in sample (**b**), and cross-sections of the distribution of thermal fields (**c**).

Table 1. Comparison of the sample temperature differences in the models with and without thermal resistance (at different powers).

№	**P, W**	**$\Delta T_{1–5}$, °C**	**$\Delta T_{1–5}$ (with Thermoresistance), °C**	**Δ, °C**
1	18.7	10	9.8	0.2
2	14.9	8	7.9	0.1
3	11.2	6	5.9	0.1
4	7.5	4	3.9	0.1

The main heat flux $\mathbf{q}_{\text{general}}$ flows through the sample from the heating unit to the cooling unit. The temperature decrease caused by thermal resistances originates in them having a direct outlet into the surrounding air; therefore, the measured heat flux is: $\mathbf{q}_{\text{total}} = \mathbf{q}_{\text{general}} - \mathbf{q}_{\text{ext}}$, which leads to a temperature gradient (Figure 7a). These considerations were used to assess the setup instrumental error, which can later be used to measure the thermal conductivity coefficient of structural and functional materials (Table 1).

A comparison of computer-modelled and experimental temperature data regarding the setup working area (at a fixed temperature difference of ΔT = 10 °C) is shown in Figure 7b. The error of the modelling results was lower than 5%, which shows the accuracy of our mathematical model of physical processes and the reliability of the obtained experimental results.

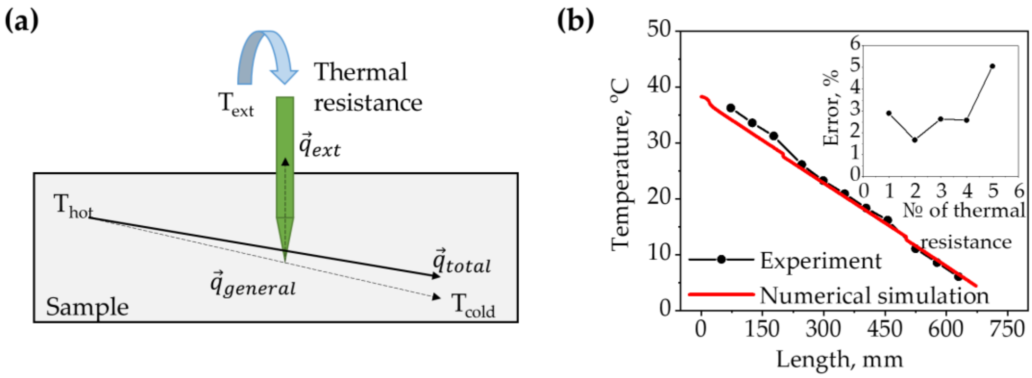

Figure 7. Changing the heat flux by introducing a thermal resistance into the sample (**a**); and comparison of computer simulation data with experimental data (**b**).

4. Setup Control System

4.1. Block Diagram

The electronic control unit of the automated system for the measurement of thermal conductivity of functional and structural products consists of a processor, auxiliary microcontrollers, high-precision analog-to-digital converters (ADCs), thermal resistances (thermoresistive temperature sensors), stepper motor drivers, and inductive end sensors (Figure 8).

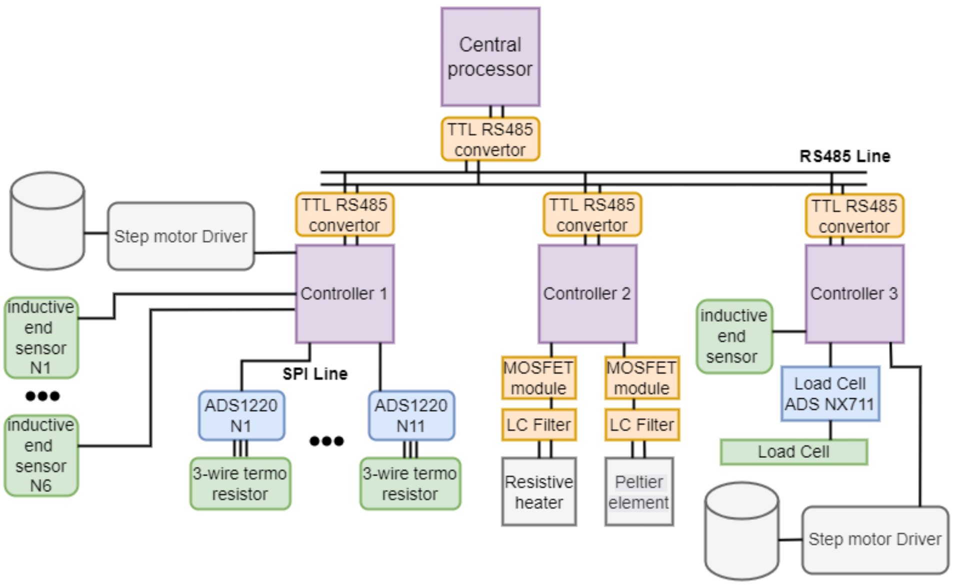

Figure 8. Block diagram of the software part of the setup.

All controllers and the processor are connected by a common data exchange bus. The central processor sequentially interrogates the auxiliary controllers, each of which sends back its data and executes the received commands. The auxiliary controllers perform different functional tasks.

Auxiliary controller 1 sequentially polls eleven ADCs and receives temperature data from thermal resistances. The data are then filtered and sent to the central processor. Additionally, the controller operates a stepper motor for clamping thermal resistances and monitors the readings of six inductive end sensors to monitor the position of thermal resistances.

Auxiliary controller 2 controls the power of heating and cooling units. Upon receiving a command from the central processor, it sets the required duty ratio of pulse width modulation (PWM) for signals received by transistor modules. The voltage from the transistor modules is smoothed out by LC filters. The smoothed voltage is applied to the resistive heater and the Peltier module, thus controlling heating and cooling, respectively.

Auxiliary controller 3 is required to control the stepper motor of the heater clamp. On a constant basis, the ADC of the clamp load cell is polled and, on receiving a command from the central processor to perform clamping and information about the required force, the controller sends signals to the stepper motor driver of the heater clamp. Upon receiving a command to remove the heater back, the controller rotates the motor until the inductive end sensor is triggered.

In order to run the setup, we developed algorithms (Figure 9) for the operation of the central (main) program and three auxiliary controllers.

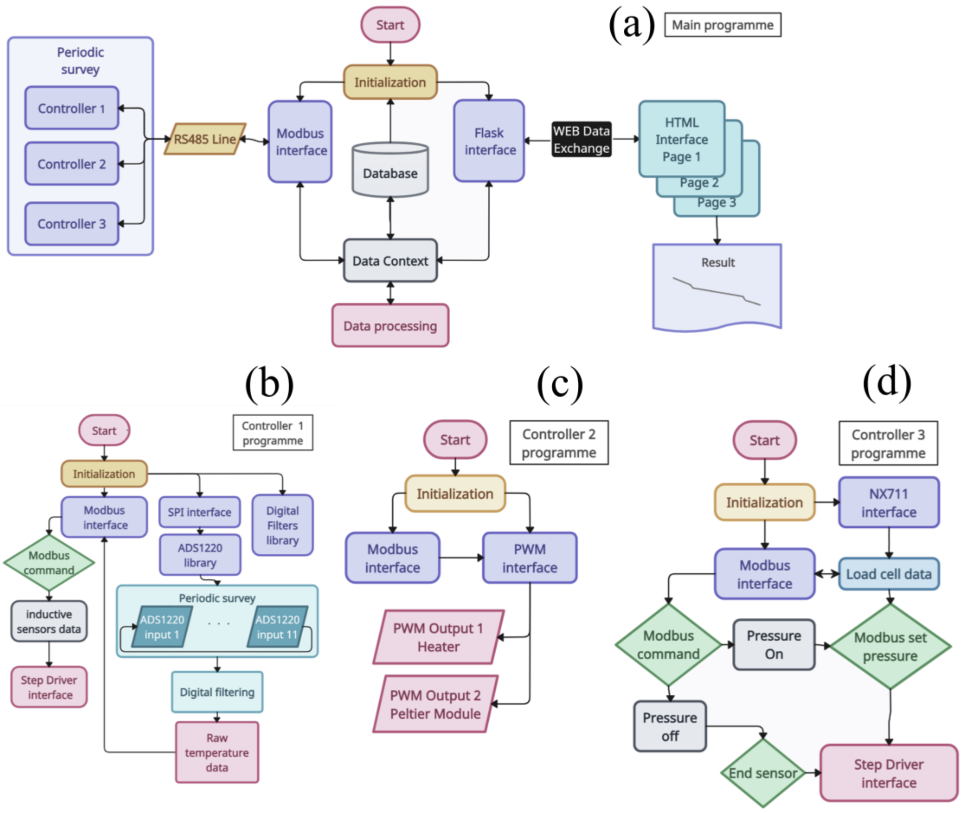

Figure 9. The program algorithm for the central (main) program (**a**), for the auxiliary controller 1 (**b**), for the auxiliary controller 2 (**c**), and for the auxiliary controller 3 (**d**).

Program for the central processor (Figure 9a). After the program starts, variables and libraries responsible for communication protocols and exchange with database are initialized. The settings of the electronic components of the system are loaded from the database. Then, the interface handler program is launched. A web interface page with controls and indicators is launched in a browser. An asynchronous processor flow performs sequential data exchange with auxiliary controllers responsible for their tasks. Data received from the web interface are stored in the general data context, which also includes data from auxiliary controllers. Then, complex data processing is performed.

The program maintains a preset heat flux in the heating and cooling units using proportional–integral–derivative (PID) controllers. After stabilization, the program plots a graph of the temperature distribution in the sample, heating unit, and cooling unit; the thermal conductivity coefficient is calculated and output.

The program of the auxiliary controller 1 (Figure 9b) works according to the following algorithm. After the program is launched and the interface and libraries are initialized, the program starts a cyclic polling of the ADCs. Their data are processed by digital filters and sent to the central processor. On command of the central processor, the controller sends control signals to the stepper motor driver to introduce thermal resistances into the sample or to remove them. Upon introducing thermal resistances, magnetic end sensors located on the thermal resistance mounts are triggered. When all five sensors are triggered, the stepper motor stops. The controller monitors errors of receiving data from the ADCs and thermal resistances and transmits the data to the central processor.

The program of the auxiliary controller 2 (Figure 9c) works according to the following algorithm. After the program is launched and the libraries are initialized, the central processor sets the level of the specified PWM output. Two PWM outputs are enabled on the controller. By varying the duty ratio of these outputs, the power of the heating and cooling units is adjusted. The PWM outputs are connected to LC filters, after which the signals are smoothed and fed to the resistive heater and the Peltier module.

The program of the auxiliary controller 3 (Figure 9d) works according to the following algorithm. After the start of the program and the initialization of the libraries, the system performs a continuous polling of the chip responsible for the digitization and transmission of data from the clamp load cell. Information on the force currently applied on the load cell is sent to the central processor and to the controller pressure unit for output. The program is responsible for receiving the command to turn on the clamp and maintains the specified clamping force. If the current force is lower than the preset one, then, the stepper motor is turned on in the forward direction to increase the clamping force. If the force is greater than the preset one, then, the motor is rotated in the opposite direction. When a command is received to turn off clamping, the controller turns on the motor in the backward direction until the magnetic end sensor is triggered.

4.2. Software Interface

After launching the software of the automated system for measuring the thermal conductivity of functional and structural products and loading the operating system, a browser opens and the main software window loads (Figure 10).

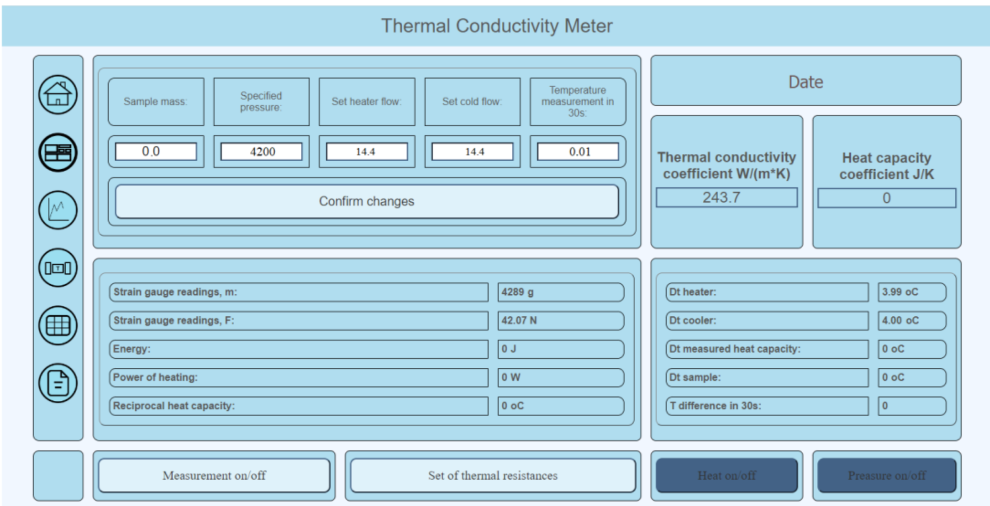

Figure 10. The software interface.

In order to measure the thermal conductivity coefficient, the user places the sample into the measurement compartment and closes it with a lid. Then, a clamping force for the heating unit and thermal resistances (to be automatically introduced into the sample) is set. Next, the required heat flux is set in the range of 7–25 W, and measurements are carried out. The obtained results are displayed in a dialog box on the screen in the form of graphs of temperature distribution in the heating block, the sample, and the cooling unit. Numerical values of the heat flux in the heating and cooling units along with the thermal conductivity coefficient are also displayed (Figure 11). The software outputs can be saved to a file. To minimize the statistical measurement uncertainty, it is recommended to conduct a series of 10 parallel experiments.

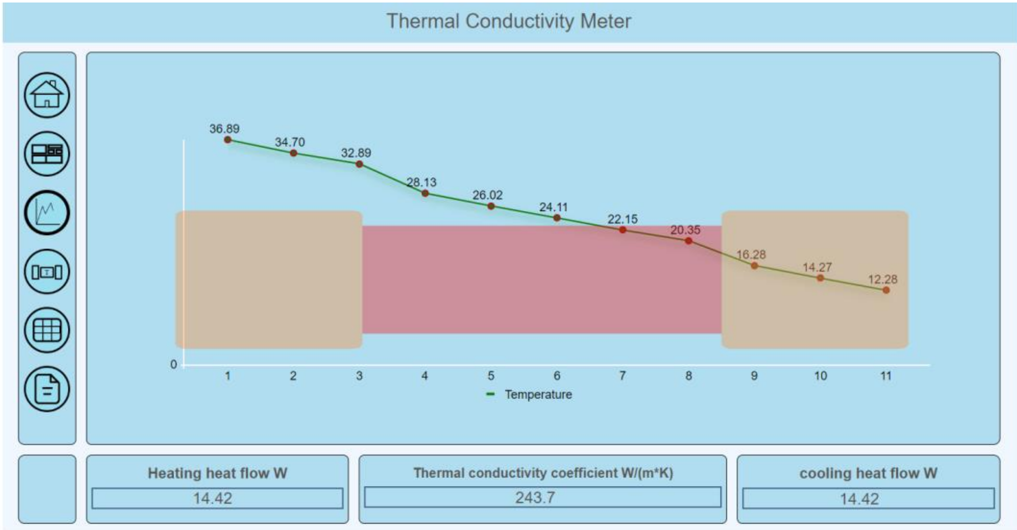

Figure 11. The software outputs.

Heat fluxes are controlled through the main program by using configured PID controllers. The related calculations are based on the difference between the readings of thermal resistances 1–3 in the heating unit and analogous thermal resistances 9–11 in the cooling unit.

The criterion for stopping the measurement is the attainment of a steady state, i.e., the equality of heat fluxes in the heating unit and the cooling unit (this takes about one hour) and the stability of the thermal conductivity coefficient readings (changes of less than 0.1% within a minute).

5. Results and Discussion

5.1. Sample Description and the Results of Its Examination

The automated system for the measurement of the thermal conductivity of functional and structural products was tested and calibrated using a reference sample of pure aluminum (99.999 wt.% Al) with a density of ρ = 2698.9 kg/m^3 at room temperature T_{room} = 22 ± 1 °C. The geometric dimensions of the aluminum bar were 40 × 40 × 300 mm. The experimental setup attained the steady state within Δt = 1 h after the heat fluxes on the heating and cooling unit were balanced.

The thermal conductivity coefficient was measured for four temperature differences $\Delta T_{1\text{-}5}$ at sample spots No. 1 and No. 5 with varying heat flux from the heating unit (Q_1) and the cooling unit (Q_2) (Table 2).

Table 2. Measurement parameters.

№	ΔT, °C	<Q_1>, W	<Q_2>, W	<λ>, W/m·K	<λ>, W/m·K
1	3.9 ± 0.1	7.3 ± 0.1	7.3 ± 0.1	246 ± 3	243 ± 3
2	6.0 ± 0.1	10.9 ± 0.1	10.8 ± 0.1	240 ± 2	
3	7.7 ± 0.1	14.4 ± 0.1	14.4 ± 0.1	244 ± 3	
4	9.8 ± 0.1	18.1 ± 0.1	18.1 ± 0.1	242 ± 2	

Figure 12, a shows the curves of temperature distribution in the sample, the heating and the cooling units, as averaged over 10 experiments. The curves have the same shape, which is in accordance with the literature data and the modelling results; the greater the slope angle of a curve, the greater the heat flux in the sample.

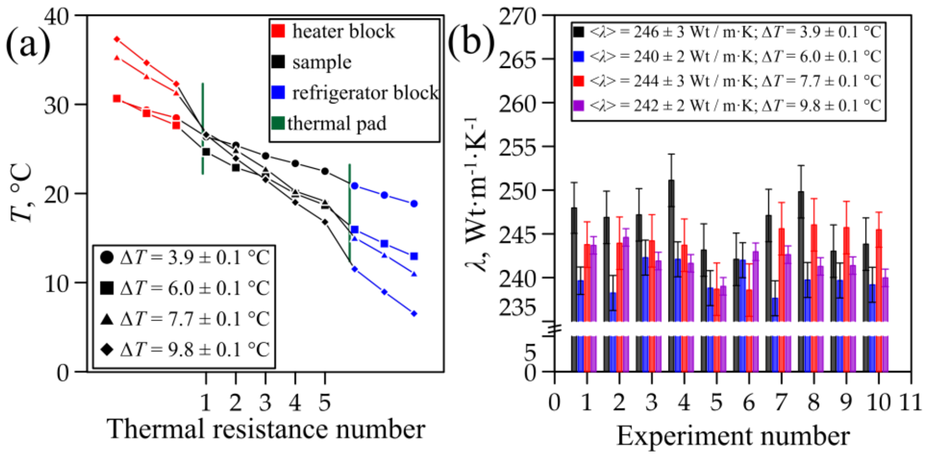

Figure 12. Temperature distribution in the setup (**a**) and repeatability of the thermal conductivity coefficient measurement results (**b**).

The experimental value of the thermal conductivity coefficient, as averaged for various temperature differences at the extremities of the sample, is <λ> = 243 ± 3 W/m·K (Figure 12b). A series of 10 tests ensures the repeatability of the results and minimizes the random measurement error. The random error of the determination of the thermal conductivity coefficient is about 1%, which demonstrates the high measurement accuracy of the developed automated system for measuring the thermal conductivity of functional and structural products.

5.2. Comparison of the Values of Thermal Conductivity of Pure Aluminum as Measured in Our Setup and by Other Methods

We compared the experimental value of the thermal conductivity coefficient of a pure aluminum sample, as measured on the above-described setup, with the results of the laser flash method as implemented in the NETZSCH LFA–467 instrument (Equation (9)) [17].

$$\lambda = \alpha \cdot \rho \cdot C_p, \tag{9}$$

where α is the temperature conductivity, ρ is density, and C_p is the heat capacity of the sample.

The ambiguity of thermal conductivity coefficient values is related to the determination of the material heat capacity. The heat capacity was studied using a NETZSCH DSC–404 C calorimeter in an inert argon medium. The experimental curve of the sample heat capacity values is shown in Figure 13b. Based on its shape and without detailing the processes occurring in the material, two values of the heat capacity can be obtained: C_{p1} = 949 J/kg·K (determined at the minimum of the functional curve, at a temperature of about 70 °C) and C_{p2} = 911 J/kg·K, obtained by an approximation of the linear, higher-temperature section of the curve down to T_{room} = 22 ± 1 °C (Figure 13a). From the two different values of the sample heat capacity, the thermal conductivity coefficients $<\lambda_1>$ = 257 ± 2 W/m·K and $<\lambda_2>$ = 247 ± 2 W/m·K can be derived (Figure 13b).

The values of the thermal conductivity coefficient, obtained in this work, were compared with known values from the literature data (Figure 14) [54].

In this work, using the newly developed automated system for measuring the thermal conductivity of functional and structural products, we measured (Figure 14) the thermal conductivity coefficient of pure aluminum (<λ> = 243±3 W/m·K at T_{room} = 22 ± 1 °C). The obtained values are consistent with the literature data [54] (falling within the range of λ = 210 ÷ 260 W/m·K) and experimental results obtained by the laser flash method ($<\lambda_2>$ = 247 ± 2 W/m·K).

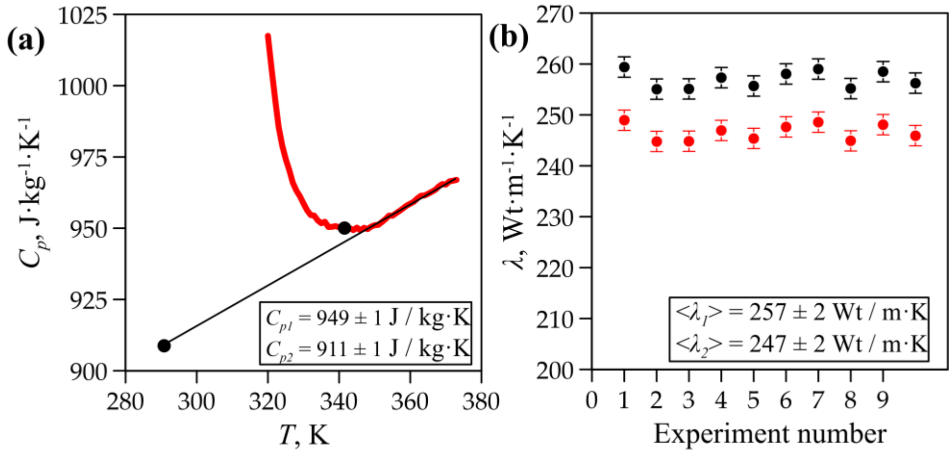

Figure 13. Heat capacity (**a**) and thermal conductivity of the sample as obtained by laser flash method (**b**).

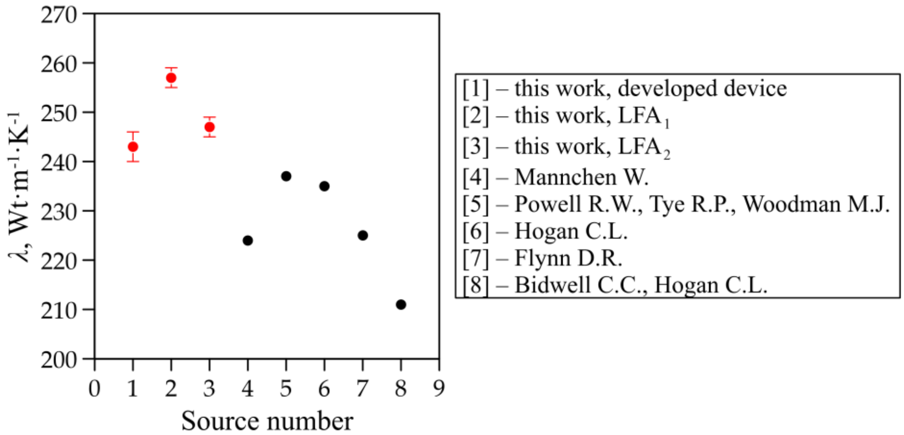

Figure 14. Comparison of thermal conductivity coefficients from this paper - developed device (1); LFA$_1$ (2); LFA$_2$ (3); and from the literature data—Mannchen W. (4); Powell R.W., Tye R.P., Woodman M.J. (5); Hogan C.L. (6); Flynn D.R. (7); Bidwell C.C., Hogan C.L. (8) [54].

6. Conclusions

The paper analyses existing steady-state and non-steady-state techniques for studying the thermal conductivity coefficients of materials.

We developed, designed, built, tested, and calibrated an automated system for measuring the thermal conductivity of functional and structural products. The system is based on a steady-state Fourier's law-based method for measuring the thermal conductivity coefficient. We described the structural elements and materials of the setup and presented its drawings.

We demonstrated the results of computer modelling of heat transfer processes involved in measuring the thermal conductivity coefficient of an aluminum sample, viz, shown the distribution of thermal fields in connection with changes in temperature differences at the extremities of the samples (ΔT); estimated the effect of the thermal conductivity coefficient of thermal pads; and detailed the change in thermal fields in the presence of thermal resistances in the sample.

The obtained experimental value of the thermal conductivity coefficient $\langle\lambda\rangle = 243 \pm 3$ W/m·K with a measurement error of about 1% is fairly consistent with the literature data ($\lambda = 210 \div 260$ W/m·K) and experimental values obtained by the laser flash method ($\langle\lambda_2\rangle = 247 \pm 2$ W/m·K).

Further studies will focus on expanding the number of measured materials: metals, such as steel, copper, and titanium; carbon materials, such as graphite and graphite foils; and silicon carbides, tungsten, and boron. We plan to improve the design of the setup in order to be able to measure thermal conductivity coefficients in the temperature range of −50…250 °C.

Author Contributions: Conceptualization, N.S.M., S.N.C. and V.V.A.; data curation, V.Y.G. and R.A.M.; formal analysis, N.S.M., V.Y.G., M.S.K. and R.A.M.; investigation, M.S.K. and R.A.M.; methodology, N.S.M., A.V.G. and S.N.C.; resources, D.V.V.; software, V.Y.G., D.V.V. and M.S.K.; supervision, S.N.C. and V.V.A.; validation, N.S.M. and A.V.G.; visualization, V.Y.G., D.V.V., M.S.K. and R.A.M.; writing—original draft, V.Y.G. and R.A.M.; writing—review and editing, N.S.M., A.V.G., S.N.C. and V.V.A. All authors have read and agreed to the published version of the manuscript.

Funding: This research received no external funding.

Data Availability Statement: The data presented in this study are available upon request from the corresponding author.

Conflicts of Interest: The authors declare no conflicts of interest.

References

1. Lou, F.; Dong, S.; Ma, Y.; Chen, X.; Zhu, K. Thermal conductivity test and model modification of SiO_2 aerogel composites based on heat flow meter method. *Appl. Therm. Eng.* **2024**, *254*, 123877. [CrossRef]
2. Yan, Y.; Zhuang, Y.; Ouyang, H.; Hao, J.; Han, X. Experimental investigation on optimization of the performance of gallium-based liquid metal with high thermal conductivity as thermal interface material for efficient electronic cooling. *Int. J. Heat Mass Transf.* **2024**, *226*, 125455. [CrossRef]
3. Braun, J.L.; Olson, D.H.; Gaskins, J.T.; Hopkins, P.E. A steady-state thermoreflectance method to measure thermal conductivity. *Rev. Sci. Instrum.* **2019**, *90*, 024905. [CrossRef] [PubMed]
4. Wang, F.; Wang, Y.; Sun, C.; Sun, C.; Zhang, P.; Xia, X. Experimental investigation on temperature-dependent effective thermal conductivity of ceramic fiber felt. *Int. J. Therm. Sci.* **2024**, *200*, 108965. [CrossRef]
5. Khandelwal, M.; Mench, M.M. Direct measurement of through-plane thermal conductivity and contact resistance in fuel cell materials. *J. Power Sources* **2006**, *161*, 1106–1115. [CrossRef]
6. Barragan, V.M.; Maroto, J.C.; Pastuschuk, E.; Munoz, S. Testing a simple Lee's disc method for estimating throuh-plane thermal conductivity of polymeric ion-exchange membranes. *Int. J. Heat Mass Transf.* **2022**, *184*, 122295. [CrossRef]
7. Xing, L.; Xie, K.; Zheng, Y.; Hou, B.; Huang, L. A thermal balance method for measuring thermal conductivity by compensation of electric cooling or heating based on thermoelectric modules. *Int. J. Therm. Sci.* **2023**, *2023*, 108264. [CrossRef]
8. Kim, D.; Lee, S.; Yang, I. Verification of thermal conductivity measurements using guarded hot plate and heat flow meter methods. *J. Korean Phys. Soc.* **2021**, *78*, 1196–1202. [CrossRef]
9. Parcesepe, E.; De Masi, R.F.; Lima, C.; Mauro, G.M.; Maddaloni, G.; Pecce, M.R. Experimental Evaluation of the Mechanical Strengths and the Thermal Conductivity of GGBFS and silica fume based alkali-activated Concrete. *Materials* **2021**, *14*, 7717. [CrossRef]
10. Kioupis, D.; Skaropoulou, A.; Tsivilis, S.; Kakali, G. Properties and durability performance of lightweight fly ash based geopolymer composites incorporating expanded polystyrene and expanded perlite. *Ceramics* **2022**, *5*, 821–836. [CrossRef]
11. Bianchi, M.; Valentini, F.; Fredi, G.; Dorigato, A.; Pegoretti, A. Thermo-mechanical behavior of novel EPDM foams containing a phase change material for thermal energy storage applications. *Polymers* **2022**, *14*, 4058. [CrossRef] [PubMed]
12. Merillas, B.; Villafane, F.; Rodriguez-Perez, M.A. Super-insulating transparent polyisocyanurate-polyurethane aerogels: Analysis of thermal conductivity and mechanical properties. *Nanomaterials* **2022**, *12*, 2409. [CrossRef] [PubMed]
13. Brzyski, P.; Glen, P.; Gladecki, M.; Ruminska, M.; Suchorab, Z.; Lagod, G. Influence of the direction of mixture compaction on the selected properties of a hemp-lime composite. *Materials* **2021**, *14*, 4629. [CrossRef] [PubMed]
14. Sanchez-Calderon, I.; Merillas, B.; Bernardo, V.; Rodriguez-Perez, M.A. Methodology for measuring the thermal conductivity of insulating samples with small dimensions by heat flow meter technique. *J. Therm. Anal. Calorim.* **2022**, *147*, 12523–12533. [CrossRef]
15. Tywoniak, J.; Calta, V.; Stanek, K.; Novak, J.; Maierova, L. The application of building physics in the design of roof windows. *Energies* **2019**, *12*, 2300. [CrossRef]
16. Pinilla-Penalver, E.; Cantero, D.; Romero, A.; Sanchez-Silva, L. Exploring the impact of the synthesis variables involved in the polyurethane aerogels-like materials design. *Gels* **2024**, *10*, 209. [CrossRef]
17. Shulyak, V.A.; Morozov, N.S.; Gracheva, A.V.; Gritskevich, M.D.; Chebotarev, S.N.; Avdeev, V.V. Anisotropy of electrical and thermal conductivity in high-density graphite foils. *Nanomaterials* **2024**, *14*, 1162. [CrossRef]
18. He, Y. Rapid thermal conductivity measurement with a hot disk sensor: Part 1. Theoretical considerations. *Thermochim. Acta* **2005**, *436*, 122–129. [CrossRef]
19. He, Y. Rapid thermal conductivity measurement with a hot disk sensor: Part 2. Characterization of thermal greases. *Thermochim. Acta* **2005**, *436*, 130–134. [CrossRef]

20. Agazhanov, A.S.; Stankus, S.V.; Savchenko, I.V.; Samoshkin, D.A. Thermal conductivity of lead and bismuth-lead eutectic melts up to 1300 K. *Nucl. Eng. Des.* **2024**, *423*, 11316. [CrossRef]
21. Cammarata, A.; Verda, V.; Sciacovelli, A.; Ding, Y. Hybrid strontium bromide-natural graphite composites for low to medium temperature thermochemical energy storage: Formulation, fabrication and performance investigation. *Energy Convers. Manag.* **2018**, *166*, 233–240. [CrossRef]
22. Zhu, P.; Zhang, Q.; Qu, S.; Wang, Z.; Gou, H.; Shil'ko, S.V.; Kobayashi, E.; Wu, G. Effect of interface structure on thermal conductivity and stability of diamond/aluminum composites. *Compos. Part A Appl. Sci. Manuf.* **2022**, *162*, 107161. [CrossRef]
23. Matsubayashi, Y.; Goto, T.; Tsuda, H.; Akedo, J. Thermal conductivity of nanocrystalline alumina films fabricated by aerosol deposition. *Ceram. Int.* **2024**, *50*, 17940–17949. [CrossRef]
24. Liao, Q.; Yan, H.; Zhao, D.; Hu, W.; Le, Q.; Chen, R.; Guo, R. Effect of Cu addition on the thermal conductivity and mechanical properties of Mg–Zn-xCu-Ce alloys. *Mater. Today Sustain.* **2024**, *27*, 100805. [CrossRef]
25. Koltsova, T.; Bobrynina, E.; Vozniakovskii, A.; Larionova, T.; Klimova-Korsmik, O. Thermal conductivity of composite materials copper-fullerene soot. *Materials* **2022**, *15*, 1415. [CrossRef]
26. Chen, Y.; Cui, Z.; Ding, H.; Wan, Y.; Tang, Z.; Gao, J. Cost-effective biochar produced from agricultural residues its application for preparation of high performance form-stable phase change material via simple method. *Int. J. Mol. Sci.* **2018**, *19*, 3055. [CrossRef]
27. Tian, J.; Wang, C.; Wang, K.; Xue, R.; Liu, X.; Yang, Q. Flexible polyolefin elastomer/paraffin wax/alumina/graphene nanoplatelets phase change materials with enhanced thermal conductivity and mechanical performance for solar conversion and thermal energy storage applications. *Polymers* **2024**, *16*, 362. [CrossRef]
28. Vetter, J.; Beneder, S.; Kandler, M.; Feyer, F.; Korner, C.; Schmidt, M. Impact of particle size distribution in the preform on thermal conductivity, Vickers hardness and tensile strength of copper-infiltrated AISI H11 tool steel. *Materials* **2023**, *16*, 2659. [CrossRef]
29. Boissonet, G.; Grosseau-Poussard, J.L.; Bonnet, G.; Pedraza, F. Development of thermal barrier coating systems from Al microparticles–Part II: Characterisation of mechanical and thermal transport properties. *Coatings* **2022**, *12*, 106. [CrossRef]
30. Zheng, Q.; Kaur, S.; Dames, C.; Prasher, R.S. Analysis and improvement of the hot disk transient plane source method for low thermal conductivity materials. *Int. J. Heat Mass Transf.* **2020**, *151*, 119331. [CrossRef]
31. Malinaric, S.; Elkholy, A. Comparison of the new plane source method to the step wise transient method for thermal conductivity and diffusivity measurement. *Int. J. Therm. Sci.* **2021**, *164*, 106901. [CrossRef]
32. Musa, C.; Zaidi, M.; Depriester, M.; Allouche, Y.; Naouar, N.; Bourmaud, A.; Baillis, D.; Delattre, F. Development of foam composites from flax gum-filled epoxy resin. *J. Compos. Sci.* **2024**, *8*, 244. [CrossRef]
33. Gioti, C.; Vasilopoulos, K.C.; Baikousi, M.; Ntaflos, A.; Viskadourakis, Z.; Paipetis, A.S.; Salmas, C.E.; Kenanakis, G.; Karakassides, M.A. Preparation properties of a composite carbon foam as energy storage EMI shield additive for advanced cement or gypsum boards. *J. Compos. Sci.* **2024**, *8*, 251. [CrossRef]
34. Pornea, A.G.; Dinh, D.K.; Hanif, Z.; Yanar, N.; Choi, K.I.; Kwak, M.S.; Kim, J. Preparations and thermal properties of PDMS-AlN-Al_2O_3 composites through the incorporation of poly (catechol-amine)-modified boron nitride nanotubes. *Nanomaterials* **2024**, *14*, 847. [CrossRef]
35. Sadouri, R.; Kebir, H.; Benyoucef, M. The effect of incorporating juncus fibers on the properties of compressed earth blocks stabilized with portland cement. *Appl. Sci.* **2024**, *14*, 815. [CrossRef]
36. Cai, Z.; Tian, M.; Zhang, G. Experimental study on the flow and heat transfer of graphene-based lubricants in a horizontal tube. *Processes* **2020**, *8*, 1675. [CrossRef]
37. Wang, S.; Wang, C.; Hussain, M.B.; Cheng, X.; Wang, Z. Study on performance improvement of sodium acetate trihydrate in thermal energy storage system by disturbance. *Processes* **2022**, *10*, 1093. [CrossRef]
38. Park, B.K.; Kim, C.-J.; Kwon, D.E.; Lee, Y.-W. Design and fabrication of partially foamed grid structure using additive manufacturing and solid state foaming. *Processes* **2020**, *8*, 1594. [CrossRef]
39. Trofimov, A.A.; Atchley, J.; Shrestha, S.S.; Desjarlais, A.O.; Wang, H. Evaluation of measuring thermal conductivity of isotropic and anisotropic thermally insulating materials by transient plane source (Hot Disk) technique. *J. Porous Mater.* **2020**, *27*, 1791–1800. [CrossRef]
40. Bohus, M.; Ba, T.L.; Hernadi, K.; Grof, G.; Konya, Z.; Erdelyi, Z.; Parditka, B.; Igricz, T.; Szilagyi, I.M. Thermal conductivity enhancement of atomic layer deposition surface-modified carbon nanosphere and carbon nanopowder nanofluids. *Nanomaterials* **2022**, *12*, 2226. [CrossRef]
41. Varady, Z.I.; Ba, T.L.; Parditka, B.; Erdelyi, Z.; Hernadi, K.; Karacs, G.; Grof, G.; Szilagyi, I.M. Experimental investigation of rheological properties and thermal conductivity of SiO_2–TiO_2 composite nanofluids prepared by atomic layer deposition. *Nanomaterials* **2022**, *12*, 3014. [CrossRef] [PubMed]
42. Ryu, M.; Batsale, J.C.; Morikawa, J. Quadrupole modelling of dual lock-in method for the simultaneous measurements of thermal diffusivity and thermal effusivity. *Int. J. Heat Mass Transf.* **2020**, *162*, 120337. [CrossRef]
43. Dell'Avvocato, G.; Bison, P.; Palmieri, M.E.; Ferrarini, G.; Palumbo, D.; Tricarico, L.; Galietti, U. Non-destructive estimation of mechanical properties in Usibor® 1500 via thermal diffusivity measurements: A thermographic procedure. *NDT E Int.* **2024**, *143*, 103034. [CrossRef]
44. Salazar, A.; Colom, M.; Mendioroz, A. Laser-spot step-heating thermography to measure the thermal diffusivity of solids. *Int. J. Therm. Sci.* **2021**, *170*, 107124. [CrossRef]

45. Incropera, F.P.; Dewitt, D.P.; Bergman, T.L.; Lavine, A.S. *Fundamentals of Heat and Mass Transfer*; John Wiley & Sons, Inc.: Hoboken, NJ, USA, 2007; 1070p.
46. Pinheiro, P.M.; Junio, J.U.; Goncalves, L.A.P.; Peixoto da Costa, J.A.; Ochoa, A.A.V.; Alves, K.G.B.; de Novaes Pires Leite, G.; Michima, S.A. Modeling and simulation of the induction hardening process: Evaluation of gear deformations and parameter optimization. *Processes* **2024**, *12*, 1428. [CrossRef]
47. Vajdi, M.; Moghanlou, F.S.; Sharifianjazi, F.; Asl, M.S.; Shokouhimehr, M. A review on the Comsol Multiphysics studies of heat transfer in advanced ceramics. *J. Compos. Compd.* **2020**, *2*, 35–43. [CrossRef]
48. Tamanna, N.; Crouch, R.; Naher, S. Progress in numerical simulation of the laser cladding process. *Opt. Lasers Eng.* **2019**, *122*, 151–163. [CrossRef]
49. Peng, Z.; Doroodchi, E.; Moghtaderi, B. Heat transfer modelling in Discrete Element Method (DEM)-based simulations of thermal processes: Theory and model development. *Prog. Energy Combust. Sci.* **2020**, *79*, 100847. [CrossRef]
50. Tong, Z.; He, Y.-L.; Tao, W.-Q. A review of current progress in multiscale simulations for fluid flow and heat transfer problems: The frameworks, coupling techniques and future perspectives. *Int. J. Heat Mass Transf.* **2019**, *137*, 1263–1289. [CrossRef]
51. Lau, K.T.; Ahmad, S.; Cheng, C.K.; Khan, S.A.; Eze, C.M.; Zhao, J. Review on Supercritical Fluids Heat Transfer Correlations, Part II: Variants of Correction Factors and Buoyancy-Related Dimensionless Variables. *Heat. Transf. Eng.* **2024**, *45*, 569–583. [CrossRef]
52. Sharma, R.; Jadon, V.K.; Singh, B. A review on the finite element methods for heat conduction in functionally graded materials. *J. Inst. Eng. India Ser. C* **2015**, *96*, 73–81. [CrossRef]
53. Muzel, D.; Bonhin, S.; Guimaraes, N.M.; Guidi, E.S. Application of the Finite Element Method in the Analysis of Composite Materials: A Review. *Polymers* **2020**, *12*, 818. [CrossRef]
54. Powell, R.W.; Ho, C.Y.; Liley, P.E. *Thermal Conductivity of Selected Materials*; National Standard Reference Data Series–National Bureau of Standards–8 (Category 5–Thermodynamic and Transport Properties); National Bureau of Standards: Gaithersburg, MD, USA, 1966; 175p. [CrossRef]